INTERNATIONAL JOURNAL FOR NUMERICAL METHODS IN FLUIDS
Int. J. Numer. Meth. Fluids 2007; **53**:851–866
Published online 23 August 2006 in Wiley InterScience (www.interscience.wiley.com). DOI: 10.1002/fld.1310

Numerical identification of flow-induced oscillation modes in rectangular cavities using large eddy simulation

G. Rubio*,†, W. De Roeck, M. Baelmans and W. Desmet

Department of Mechanical Engineering, K.U. Leuven, Celestijnenlaan 300B, B-3001, Leuven, Belgium

SUMMARY

Self-sustained oscillations are present in a wide variety of flows. For flows passing cavities, acoustics can play a role in the physical mechanisms triggering and maintaining the oscillation phenomena. This is the case for the flow over rectangular cavities, which is studied in this paper. The compressible LES Navier–Stokes equations are solved for cavities with an upstream laminar boundary layer. The flow passing rectangular cavities is computed, varying two different parameters related to the physics of the problem, Mach number and length of the cavity divided by the momentum thickness of the boundary layer at the leading edge. This paper intends to prove that the switch between shear-layer oscillation mode, characterized by an acoustic feedback process, and wake oscillation mode, characterized by a large-scale vortex shedding with Strouhal number independent of Mach number, can be identified using large eddy simulation, and consequently, with much less computational effort than in other studies in literature, where direct numerical simulation has been applied. Copyright © 2006 John Wiley & Sons, Ltd.

Received 21 February 2006; Revised 13 June 2006; Accepted 19 June 2006

KEY WORDS: large eddy simulation; cavity flow; self-sustained oscillations

1. INTRODUCTION

The phenomenon of flows passing over a cavity has been studied in numerous investigations in the past and has a broad range of applications. These include, but are not limited to, automotive industry, gas transport systems, aircraft wheel and weapon bays and aerospace applications. The noise spectrum of cavity noise contains both broadband components, introduced by the turbulence in the shear layer, and tonal components. The latter can be induced by two mechanisms: a wake

*Correspondence to: G. Rubio, Department of Mechanical Engineering, K.U. Leuven, Celestijnenlaan 300B, B-3001, Leuven, Belgium.
†E-mail: gustavo.rubio@mech.kuleuven.be

Contract/grant sponsor: Institute for the Promotion of Innovation by Science and Technology

mode mechanism, due to a periodical vortex shedding at the cavity leading edge, and a shear-layer mode mechanism, due to a feedback coupling between the flow field and the acoustic field.

Rossiter [1] was one of the first researchers who described the feedback mechanism based on shadowgraphic observations on a number of different rectangular cavities. Based on experimental results, Rossiter derived the following semi-empirical formula for the dimensionless frequencies (Strouhal number, *St*) of this periodic phenomenon:

$$St = \frac{fL}{U_\infty} = \frac{n - \gamma}{M + 1/k} \tag{1}$$

with f the frequency, L the length of the cavity, U_∞ the free-stream velocity, n the mode number, $M = U_\infty/c_0$ the undisturbed Mach number, c_0 the speed of sound, $k = U_{\text{conv}}/U_\infty$ the ratio of the convection velocity of the vortices U_{conv} to the free-stream velocity U_∞ and γ a factor to account for the lag time between the passage of a vortex and the emission of a sound pulse at the trailing edge of the cavity.

Yet another mode of oscillation has been observed. In incompressible experiments, Gharib and Roshko [2] observed that when the length to depth ratio of the cavity was increased, the flow becomes more violent and unsteady. A big vortex that fills the whole cavity is formed at the leading edge and is ejected out of the cavity at the trailing edge when it is big enough. The flow above the cavity is, in this case, affected by the flow inside the cavity and freestream fluid is periodically going in and out of the cavity. Gharib and Roshko used the term wake mode to describe this flow regime, since the flow over the cavity looks like the wake behind a bluff body. Flow features of this mode are qualitatively very different from shear-layer mode. Numerical studies [3] show that, in wake mode, the frequencies of oscillation are independent of Mach number, suggesting the absence of a flow-acoustic coupling.

Experimental cavity flow research is dominated by the study of near-field flow features and cavity-wall pressure fluctuations. Several reviews of these experimental results are given in literature [4–7].

From the computational point of view, many studies about cavity flow exist in the literature. Recently, shear-layer and wake modes, have been numerically investigated by several authors using 2D direct numerical simulation [3, 8, 9], in the frame of aeroacoustic research. In these cases, the computational domain includes the propagation region of acoustic waves generated at the cavity. However, the different modes of oscillation can have implications in several aspects other than a different noise generation pattern. Indeed, different oscillation modes mean also different cavity drags, different boundary layer behaviours and different pressure coefficients in the walls of the cavity. In these cases, the computational domain can be smaller, and the number of turbulent scales that are resolved can be reduced, decreasing the computational cost. Also, when aeroacoustics hybrid techniques [10], where the source region and the propagation region are computed separately, are applied, the computational effort needed to compute the source region can be dramatically decreased in the same two ways stated above. First, the computational domain where the Navier–Stokes equations are solved, is reduced to the region where acoustic waves are generated. Given the small size of the domain, special care has to be taken at the boundaries by using non-reflecting boundary treatments and buffer zones. Second, in this work the main interest is to capture the right frequencies for aeroacoustic tonal noise sources, that are given by the big, energy containing eddies. Because of this, and even if turbulence is a 3D phenomenon, there is no need to accurately resolve turbulence up to the smallest scales, and hence, the use of 2D LES is justified, as well as a relatively simple subgrid scale model, provided that it does not affect the

DOI: 10.1002/fld

correct resolution of the big scales. These LES computations carried out in a smaller domain, are in time and resources, much less demanding than the DNS computations usually performed in direct numerical aeroacoustics (the DNS computations that are going to be used for comparison in this paper are also 2D [3]), and the results can be easily coupled to propagation codes, or can be used to define sources that can predict the sound pressure levels at different points in the far field using integral methods. In any of these cases, hybrid aeroacoustics techniques or looking at flow features other than noise, the cost of a direct numerical simulation is not justified.

In this paper, different oscillation regimes and transition parameters are identified using large eddy simulation. To test the ability of this methodology to extract useful acoustic information from the source region, and to distinguish between an oscillation mode where flow-acoustic interaction is happening (shear-layer mode), and another one where the oscillation frequency is fixed and independent of Mach number, and hence, of compressibility or acoustic effects (wake mode), two series of computations have been done, varying two critical parameters in the transition between shear-layer mode and wake mode.

This paper is structured as follows. In the next section, the numerical method is described and some details about the implementation are given. The test case and the parameters of the different computations are also introduced here. In Section 3 numerical results are presented and the features of the different oscillation modes are commented. The frequencies obtained are compared with DNS results. Finally in Section 4 conclusions are drawn.

2. NUMERICAL METHOD

2.1. Filtered compressible Navier–Stokes equations

The 2D compressible large eddy simulation equations for a viscous flow are obtained from a decomposition of the variables of the Navier–Stokes equations (ρ, u_i) into a Favre-filtered part ($\overline{\rho}$, $\widetilde{u}_i$) and an unresolved part (ρ', u_i') that has to be modelled with a subgrid scale model:

$$\frac{\partial \overline{\rho}}{\partial t} + \frac{\partial \overline{\rho}\widetilde{u}_i}{\partial x_i} = 0 \tag{2}$$

$$\frac{\partial \overline{\rho}\widetilde{u}_i}{\partial t} + \frac{\partial \overline{\rho}\widetilde{u}_i\widetilde{u}_j}{\partial x_j} = -\frac{\partial \overline{p}}{\partial x_i} + \frac{\partial(\widetilde{\tau}_{ij} + \tau_{ij,\mathrm{SGS}})}{\partial x_j} \tag{3}$$

$$\frac{\partial \overline{\rho}\widetilde{e}}{\partial t} + \frac{\partial \overline{\rho}\widetilde{e}\widetilde{u}_i}{\partial x_i} = -\frac{\partial \widetilde{u}_i \overline{p}}{\partial x_i} + \frac{\partial \widetilde{u}_i(\widetilde{\tau}_{ij} + \tau_{ij,\mathrm{SGS}})}{\partial x_j} - \frac{\partial(\widetilde{q}_i + q_{i,\mathrm{SGS}})}{\partial x_i} \tag{4}$$

In Equations (2)–(4), $\overline{\rho}$, $\widetilde{u}_i$ and $\overline{p}$ are the resolved density, velocity components and pressure. For a perfect gas, the total energy per mass unit $\widetilde{e}$ is defined as

$$\widetilde{e} = \frac{\overline{p}}{(\gamma - 1)\overline{\rho}} + \frac{(\widetilde{u}_i\widetilde{u}_i)}{2} \tag{5}$$

and γ is the ratio of specific heats. The viscous stress tensor $\widetilde{\tau}_{ij}$ is modelled as a Newtonian fluid, and the heat flux $\widetilde{q}_i$ is modelled with Fourier's law. Dynamic molecular viscosity and molecular conductivity are kept constant.

DOI: 10.1002/fld

The subgrid scale stress tensor $\tau_{ij,\mathrm{SGS}}$, and the subgrid scale heat flux $q_{i,\mathrm{SGS}}$, reproduce the dissipative effects of the unresolved scales by using a turbulent viscosity μ_t, and a turbulent Prandtl number Pr_t. These are then modelled as

$$\tau_{ij,\mathrm{SGS}} = 2\mu_t \widetilde{S}_{ij} \tag{6}$$

and

$$q_{i,\mathrm{SGS}} = -\frac{\mu_t c_p}{Pr_t}\frac{\partial \widetilde{T}}{\partial x_i} \tag{7}$$

with $\widetilde{T}$ the temperature and

$$\widetilde{S}_{ij} = \frac{1}{2}\left(\frac{\partial \widetilde{u}_i}{\partial x_j} + \frac{\partial \widetilde{u}_j}{\partial x_i}\right) \tag{8}$$

For the turbulent Prandtl number, a constant value of 0.5 has been chosen based on the dynamic computations of several authors. Lessani [11] found that in a channel flow LES computation using the dynamic Smagorinsky model, Pr_t stabilizes at a value of approximately 0.5 for y^+ larger than 10, and he recommends, for computations using the Smagorinsky model with constant coefficients, to use values between 0.5 and 1. The same results in a channel flow computation are reported by Moin *et al.* [12]. In the same reference it is also shown that, in several numerical experiments carried out in order to test the performance of the dynamic model for compressible isotropic turbulence decay, the turbulent Prandtl number takes values in between 0.4 and 0.8.

To determine the turbulent viscosity, a Smagorinsky model is used, where

$$\mu_t = \overline{\rho}(C_s\Delta)^2\sqrt{2\widetilde{S}_{ij}\widetilde{S}_{ij}} \tag{9}$$

The filter size Δ is locally set to the mesh size.

To take into account the scale reduction that occurs near walls, the filter size Δ is weighted with the normal wall coordinate y^+ in the way proposed by Van Driest [13]:

$$\Delta' = \Delta(1 - \exp(-y^+/A)) \tag{10}$$

This is a quite primitive way to deal with near-wall flow. However, this choice is made because it is a simple and low computational cost way of resolving the flow, provided $y^+ \approx 1$ in the first node off the wall. Also, since the incoming boundary layers, whose correct representation at the leading edge of the cavity is crucial in order to capture the right oscillation mode, are laminar, the use of more sophisticated approaches like the WALE model [14] or dynamic procedures [15], in order to find a more correct representation of the Reynolds shear stresses near the wall, are not justified.

2.2. Numerical implementation

The filtered compressible Navier–Stokes equations are implemented in a finite volume code. They are integrated in time using a fourth-order explicit Runge–Kutta scheme. Convective and viscous terms are discretized using central second-order schemes. On all solid walls, isothermal, no-slip and no-penetration conditions are imposed, with $\partial p/\partial n = 0$, n being the direction normal to the wall. At the upstream boundary, characteristic soft inflow conditions, proposed by Kim and Lee [16], are applied. At the outlet, the subsonic characteristic outflow condition of Poinsot and Lele [17],

DOI: 10.1002/fld

together with progressive mesh stretching and a sponge zone to dissipate vortical structures [18] is implemented. In this sponge zone, terms of the form

$$-\frac{c_0\sigma(x)}{\Delta x}(\mathbf{U}-\mathbf{U}_{\text{target}}) \tag{11}$$

are added to the right-hand side of Equations (2)–(4) (with $\mathbf{U}$ the vector of conservative dependent variables). The damping factor, $\sigma(x)$, varies smoothly from zero at the edge of the buffer to a constant value at the outlet following the expression:

$$\sigma(x)=\sigma_{\max}\left(\frac{x-x_0}{x_{\max}-x_0}\right)^{\alpha} \tag{12}$$

where x_0 and $x_{\max}$ are the origin and the end of the sponge zone and $\sigma_{\max}$ and α are tuning coefficients which values depend on the number of cells in the sponge region. The top boundary of the domain can be assumed to be far enough from the region where the flow is perturbed by the cavity. A free boundary condition is implemented with the derivatives of all primitive variables in the direction normal to this boundary imposed to be zero.

2.3. Numerical setup

Figure 1 shows a sketch of the computational domain and indicates several system parameters, which have been varied in 10 different cases listed in Table I.

Two main series have been computed. A similar notation is used as in the study of Rowley [3]. In the 'L' series computations, the depth of the cavity is kept constant, and the parameters L/D and L/θ_0, with θ_0 the momentum thickness of the boundary layer at the upstream edge for the initial condition, are varied. In the '$4M$' series, Mach number is varied keeping all the other parameters constant. The Reynolds number based on the cavity depth (Re_D) is 1500 in all cases. A structured multi-block mesh, consisting of two blocks, is used for the computations. The first block takes the part of the domain outside the cavity and the second one the cavity itself. This mesh is stretched in the shear layer region and towards the walls. Figure 2 shows a detail of the mesh around the leading edge. Note that cases $L4$ and $4M6$ are the same. All cases were computed with $C_s=0.1$, since this is a value that is typically used for wall-bounded flows [19], except $4M5u$ that was

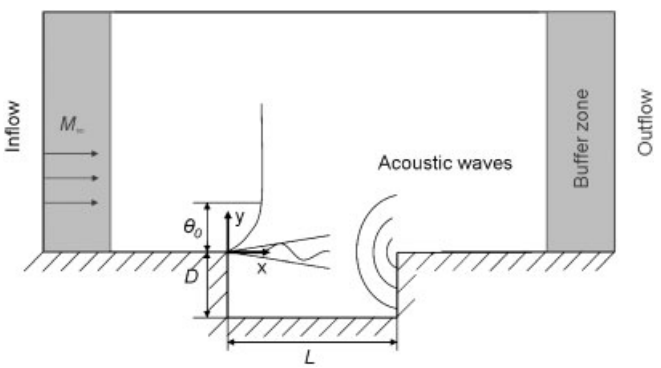

Figure 1. Cavity configuration and computational domain.

DOI: 10.1002/fld

Table I. Parameters of the different computations.

Run	L/D	M	L/θ_0	Mesh	Mode
$L2$	2	0.6	52.8	600×130 100×50	Shear
$L3$	3	0.6	75.0	650×130 150×50	Mixed
$L4$	4	0.6	102.0	700×130 200×50	Wake
$4M2$	4	0.2	102.0	700×130 200×50	Shear
$4M3$	4	0.3	102.0	700×130 200×50	Mixed
$4M4$	4	0.4	102.0	700×130 200×50	Mixed
$4M5$	4	0.5	102.0	700×130 200×50	Wake
$4M5u$	4	0.5	102.0	700×130 200×50	Wake
$4M6(L4)$	4	0.6	102.0	700×130 200×50	Wake

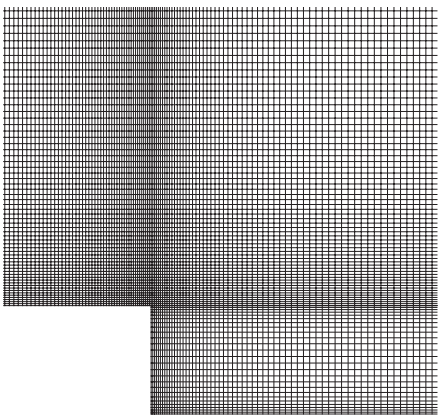

Figure 2. Mesh detail around the leading edge.

run with $C_s = 0$ (unresolved DNS). The computations are started from a laminar flat-plate Blasius boundary layer spanning the cavity, and are run until statistically steady state is reached.

3. NUMERICAL RESULTS

In this section the results of the computations are presented, and it is shown that 2D large eddy simulation in a reduced domain, is suitable for identification of different oscillation regimes and to extract tonal acoustic information.

3.1. Mesh size

Taking the cavity depth, D, as the characteristic length of the bigger scales, the Kolmogorov length scale can be estimated as

$$\frac{D}{l_\eta} \sim \frac{D}{\nu^{3/4}\varepsilon^{-1/4}} \sim \frac{D}{\nu^{3/4}(u^3/D)^{-1/4}} \sim Re_D^{3/4}$$

DOI: 10.1002/fld

The mesh that is used in the present study is approximately of size $\delta \sim 8l_\eta$. For DNS, the mesh size has to be $\delta \leqslant 2l_\eta$. The mesh used is quite close to that limit, but still belongs to the LES range (*challenging* LES is done when $\delta \sim 20l_\eta$ or bigger), hence the subgrid scale model is used.

3.2. Shear-layer mode

The shear-layer mode is characterized by the roll-up of vorticity in the shear layer, impingement and scattering of acoustic waves at the downstream cavity edge, upstream acoustic wave propagation, and receptivity of the shear layer to acoustic disturbances. These features appear clearly in the computational results. Figure 3 shows, for run $L2$, vorticity and pressure contours at three different instants, corresponding, approximately, to $\frac{1}{3}$ phase intervals of the second Rossiter mode, which is dominant for this computation. The vorticity contours show a steady vortex occupying the rear half of the cavity, evidencing that the interaction of the shear layer with the flow inside the cavity is very weak for this mode of oscillation. The pressure contours allow to identify what will be the directivity of the acoustic field propagated upstream far from the cavity. The regions in the cavity with negative values of the pressure fluctuations, are the result of the swirling movement of the stationary vortex.

3.3. Wake mode

As the length of the cavity, relative to the momentum thickness of the boundary layer at the leading edge, or the Mach number are increased, there is a substantial change in the pattern of the cavity oscillations. Under these conditions, the flow is characterized by a large-scale vortex shedding from the cavity leading edge. The vortex reaches nearly the cavity size, dragging during his formation irrotational free-stream fluid into the cavity. The vortex is then shed from the leading edge, and violently ejected from the cavity. Note that in this case the boundary layer undergoes separations, upstream during the vortex formation, and downstream, as it is convected away. These events are clearly visible in Figure 4. In this case there are two reasons for the low pressure regions in the cavity. One of them is, as in the shear-layer mode, the vortical swirling motion in the cavity, but also the expansion that the flow undergoes in the first half of the cavity, as the big vortex is ejected.

In Figures 3 and 4, some discontinuities can be appreciated in the line where the two blocks of the mesh are connected. This is due to the fact that the cell-centred approach is used in the finite volume formulation of the CFD code. Because of this, the visualization software has to extrapolate values of the primitive variables from the cell centres to this line, which is common for both blocks. This is done using values above the cavity for block 1, and inside the cavity for block 2. Because of this, two slightly different values are obtained on this line, and hence a discontinuity appears.

3.4. Flow features

Figure 5 shows time-averaged streamlines for computations $L2$ (shear-layer mode) and $4M5$ (wake mode). The streamlines above the cavity are clearly deflected in the wake mode, whereas the shear-layer mode shows mean flow streamlines nearly horizontal along the mouth of the cavity.

Similar flow features can be seen in the streamwise velocity profiles in Figure 6, for cavities $4M2$ (shear-layer mode) and $4M5$ (wake mode). The oscillations in wake mode have a significant impact on the mean flow outside the cavity. It is important to remark that they affect the pattern of this mean flow even in the upstream direction. Due to this, the momentum thicknesses at the

DOI: 10.1002/fld

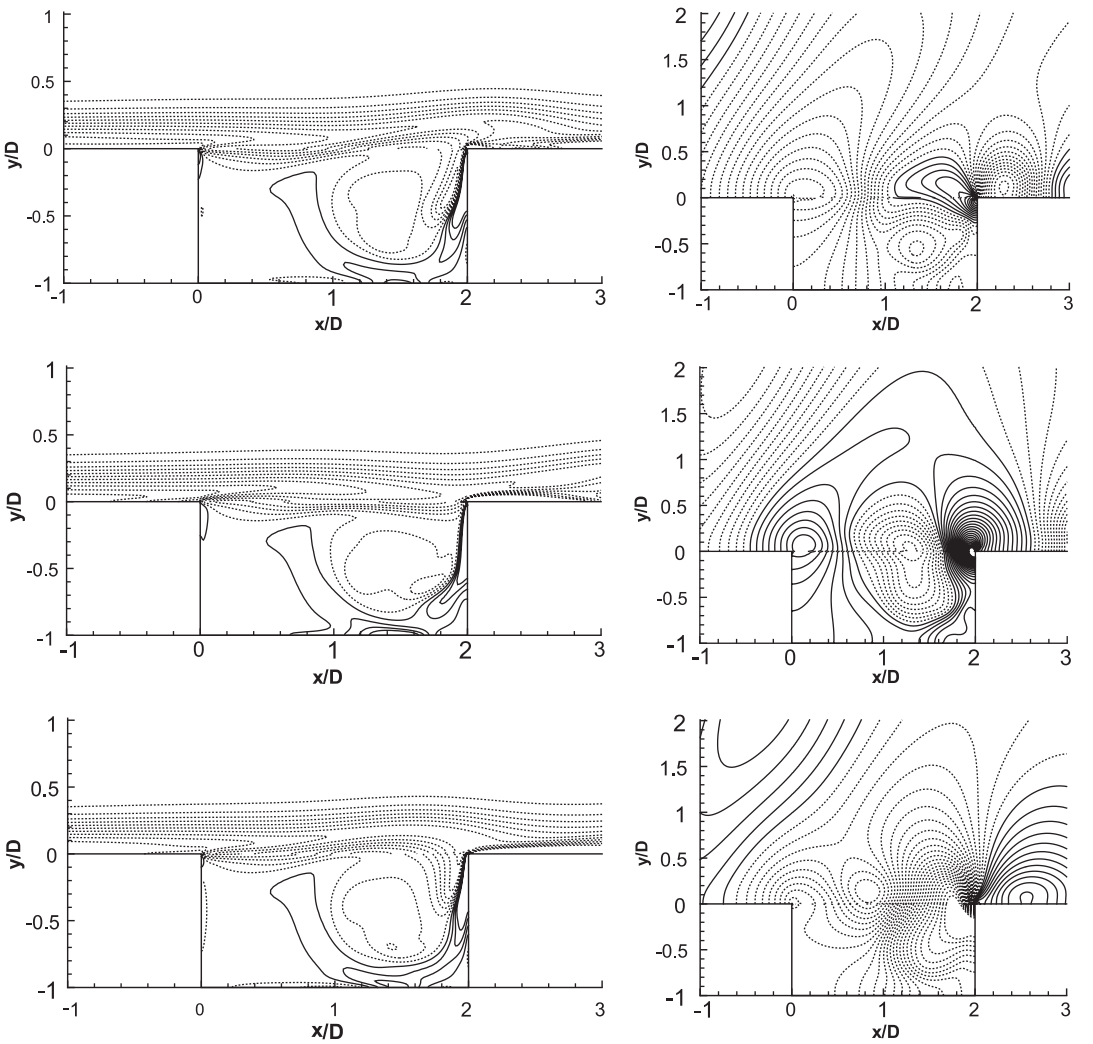

Figure 3. Cavity $L2$. Shear layer mode. On the left, vorticity field during one cycle of oscillation (Second Rossiter mode). 15 contours of $\omega D/U$ are shown between -5 and 1.67. On the right, pressure fluctuation contours are shown at the same instants. 50 contours of $(p - p_\infty)/\rho U_\infty^2$ are shown between -0.06 and 0.06. Negative contours are dashed in both cases.

leading edge that are imposed as initial conditions are substantially different from those that are found in the statistically converged flow. In the shear-layer mode, only the flow field in the rear half of the cavity is significantly modified from the initial solution.

The Reynolds stresses, defined as

$$u_{\text{rms}} = \frac{\sqrt{\langle u'^2 \rangle}}{U_\infty}, \quad v_{\text{rms}} = \frac{\sqrt{\langle v'^2 \rangle}}{U_\infty}, \quad uv_{\text{rms}} = \frac{\sqrt{\langle |u'v'| \rangle}}{U_\infty} \tag{13}$$

DOI: 10.1002/fld

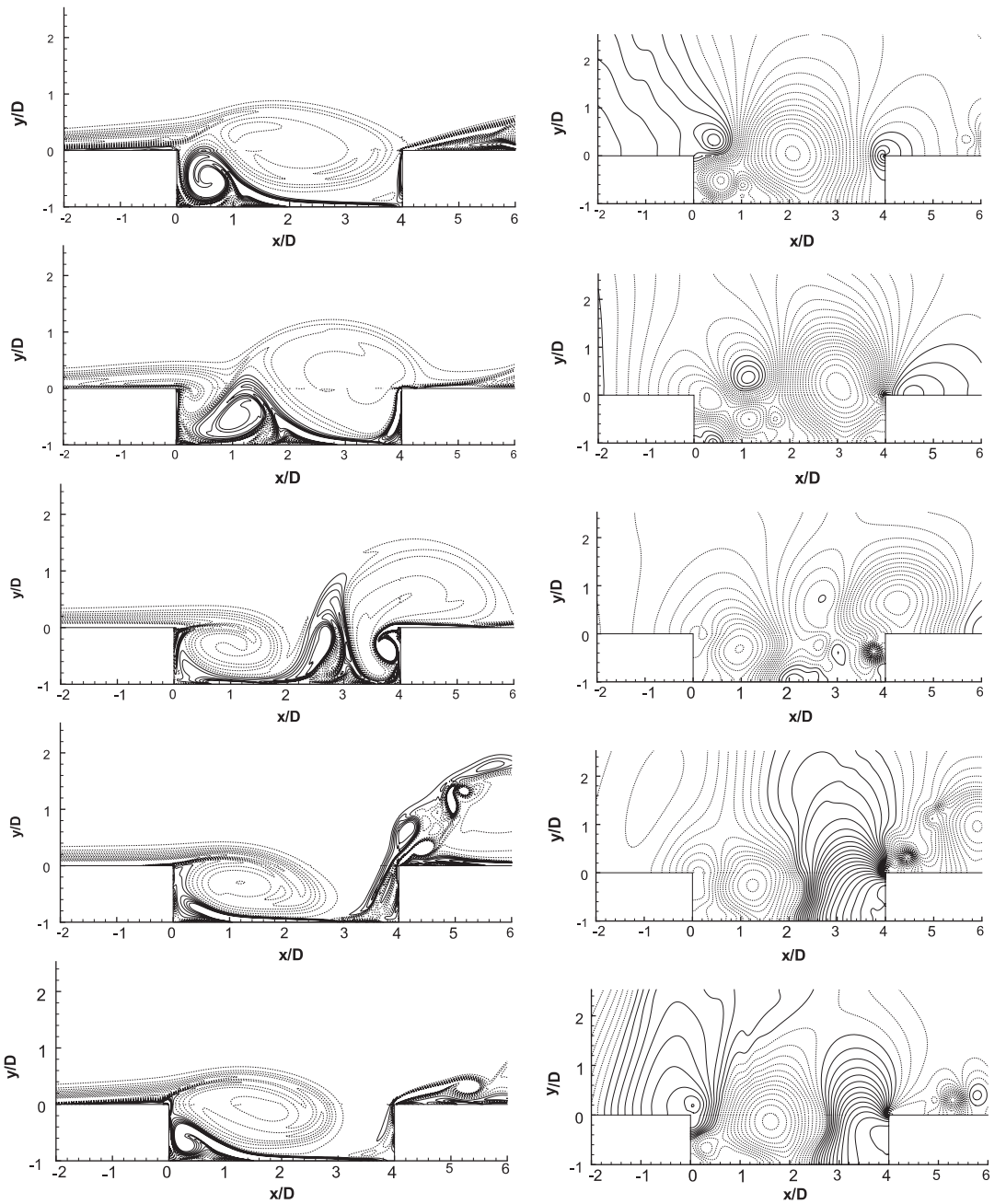

Figure 4. Cavity $4M6$ ($L4$). Wake mode. On the left, vorticity field during one cycle of oscillation. 16 contours of $\omega D/U$ are shown between -5 and 3. On the right, pressure fluctuation contours are shown at the same instants. 50 contours of $(p - p_\infty)/\rho U_\infty^2$ are shown between -0.7 and 0.7. Negative contours are dashed in both cases.

DOI: 10.1002/fld

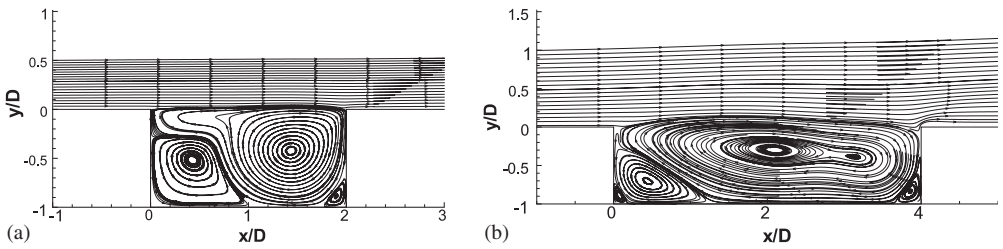

Figure 5. Time averaged streamlines for: (a) $L2$ (shear-layer mode); and (b) $4M5$ (wake mode).

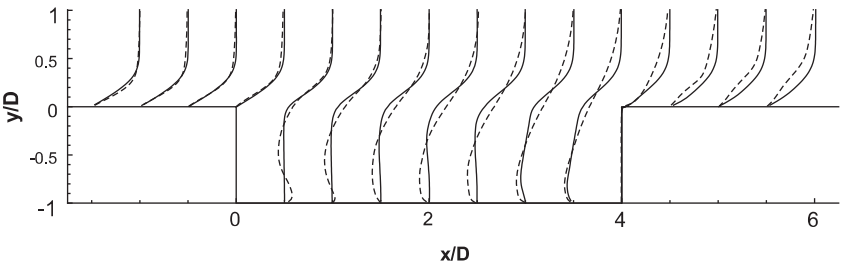

Figure 6. Statistically converged streamwise velocity profiles, $\langle u \rangle / U_\infty$ at different positions for runs $4M2$ (shear-layer mode, solid) and $4M5$ (wake mode, dashed).

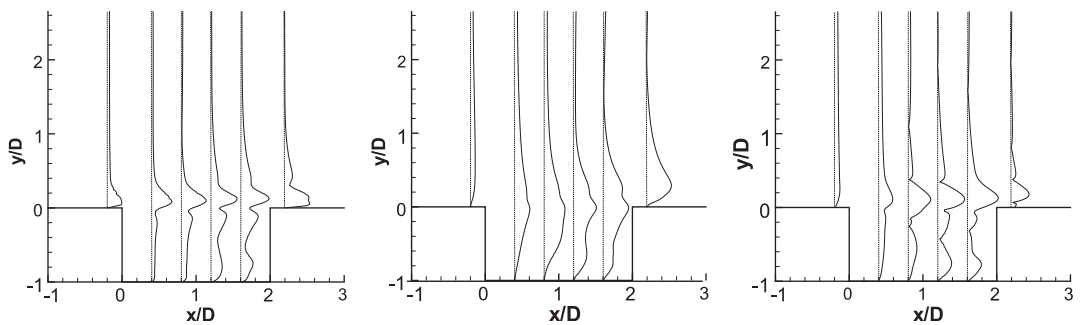

Figure 7. Reynolds stresses profiles for cavity $L2$. From left to right u_{rms}, v_{rms} and uv_{rms}.

are shown in Figure 7 for the cavity $L2$. Note that in the profiles of u_{rms}, towards the second half of the cavity a double peak is observed, as reported in the experiments of Ziada and Rockwell [20] about the interaction of a mixing layer with a corner.

Sarohia [21] observed experimentally a level of fluctuations of the order of 0.15 close to the trailing edge. For a mixing layer, typical values between 0.16 and 0.18 for u_{rms}, and between 0.12 and 0.14 for v_{rms} are found in literature. In the reported computation $L2$, the maximum value of u_{rms} is 0.092 and of v_{rms}, 0.125. This mismatch in u_{rms} might be due to the fact that only second-order schemes are used in these calculations. Because of this low-order, and since a clear identification of the tones associated with the Rossiter frequencies was envisaged, conservative mesh sizes have

DOI: 10.1002/fld

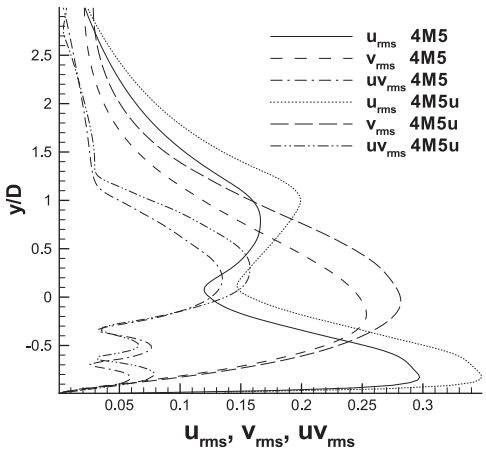

Figure 8. u_{rms}, v_{rms} and uv_{rms} at location $x = 3D$ from the leading edge for runs $4M5$ ($C_s = 0.1$) and $4M5u$ (unresolved DNS).

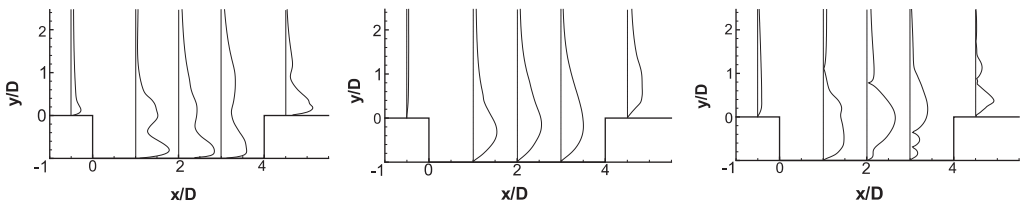

Figure 9. Reynolds stresses profiles for cavity $4M5$. From left to right u_{rms}, v_{rms} and uv_{rms}.

been used. This means that the mesh is almost the size of a DNS mesh, making the computations very sensitive to an overdissipation of turbulent kinetic energy, even for small values of C_s. This becomes more evident in Figure 8, where the profiles of u_{rms}, v_{rms} and uv_{rms} are compared for the runs $4M5$ ($C_s = 0.1$) and $4M5u$ (unresolved DNS) at location $x = 3D$ from the leading edge. For the three profiles, the stresses differ about 15% between the cases with $C_s = 0.1$ and 0. In the opinion of the authors, this means that the rate of strain tensor that is resolved by using this mesh is quite high and possibly the cutoff wave number is located very close to the dissipation zone of the energy spectrum, making the computation very sensitive to an overdissipation of energy. The results could probably be improved by using a dynamic procedure [15].

The Reynolds stresses at different x/D locations, for a cavity oscillating in wake mode ($4M5$) are shown in Figure 9. These are clearly different from the ones shown in Figure 7 (shear mode).

3.5. Frequencies of oscillation

For every run, the time signals of the primitive variables have been recorded at a point in the cavity mouth located at $x = L - 0.87D$ (Figure 10). In the spectrum of every case, several distinct tonal peaks and their harmonics become apparent.

DOI: 10.1002/fld

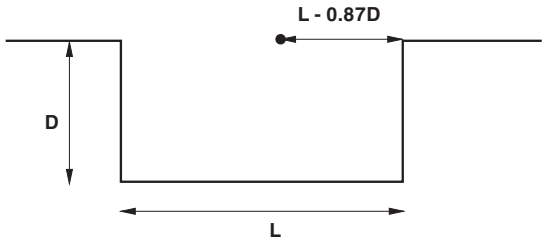

Figure 10. Location of the monitoring point.

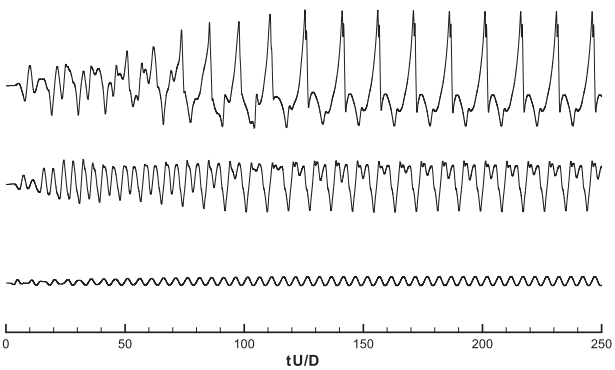

Figure 11. Time series of the normal velocity in the cavity mouth, at $x = L - 0.87D$, for the runs $L2$, $L3$ and $L4$ (from bottom to top). The relative amplitude of the fluctuations has been kept unmodified for comparison.

Time traces of the normal velocity at the point given above are shown in Figure 11 for the 'L' series, where L/θ_0 is varied for constant D. By comparison with the results of Rowley [3], cases $L2$ and $L4(4M6)$ can be clearly identified as shear mode and wake mode, respectively. For the case $L3$ ($L/\theta_0 = 75$), it appears that both modes are present at the same time, marking a transition point.

Several runs of the series '$4M$', where Mach number is changed, keeping all the other parameters constant, are plotted in Figure 12. For run $4M2$ there is a very small oscillation that is almost not visible in comparison with the other cases meaning that, for this computation, since the amplitude of the oscillations is considerably smaller than in the other cases in the '$4M$' series, the mesh should have been refined in the shear layer region. On the other hand, $4M6(L4)$ is a wake mode, as explained in the previous paragraph. Cavities $4M3$ and $4M4$, seem to show both modes of oscillation, being $4M3$ closer to shear-layer mode, and $4M4$ closer to wake mode. It could be said that Mach numbers 0.3 and 0.4 mark the transition zone between shear mode and wake mode. For $4M4$, Rowley predicts already full transition to wake mode. This discrepancy can be due, again, to the fact that only second-order schemes are used, which might be not accurate enough to capture the right features of the flow, when the combination of parameters is such that the flow is close to the transition point between shear-layer mode and wake mode. For this reason the run $4M4$ is labelled as mixed mode in Table I.

DOI: 10.1002/fld

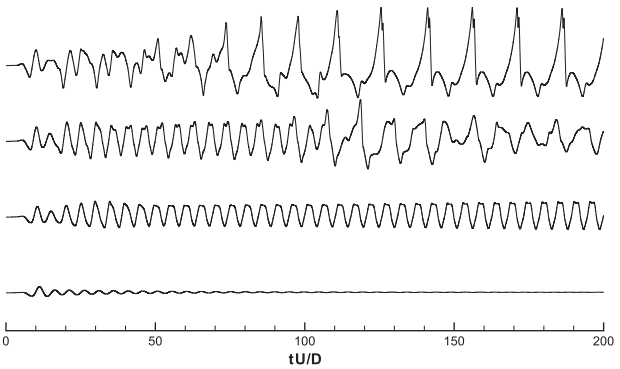

Figure 12. Time series of the normal velocity in the cavity mouth, at $x = L - 0.87D$, for the runs $4M2$, $4M3$, $4M4$ and $4M6$ (from bottom to top). The relative amplitude of the fluctuations has been kept unmodified for comparison.

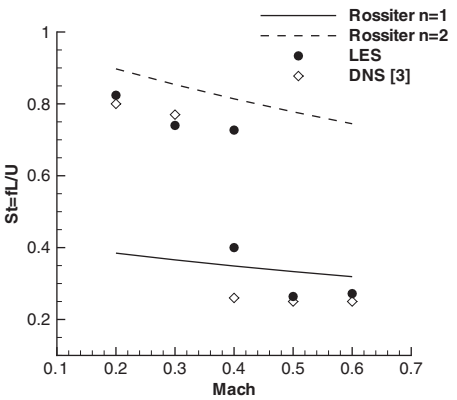

Figure 13. Strouhal numbers for peaks in spectra for the $4M$ series of runs, compared to Equation (1) and to DNS results [3].

The transformation of the data to the frequency domain confirms the identification of the oscillation mode for every cavity. In Figure 13, the frequencies of the most dominant peaks in the spectra for the series of runs '$4M$' are compared with the Rossiter equation (1), with $\gamma = 0.25$ and $k = 0.57$ and with DNS results [3].

For the case $4M4$, in contrast with the others, the time signal is very noisy and it is difficult to appreciate any periodicity. For this cavity, two very energetic peaks are found in the spectra as can be seen in Figure 14(a). The spectrum for the case $4M3$ (mixed mode) is shown in the same picture, where the peaks corresponding to the second Rossiter mode and its higher harmonics are clearly visible. Note that in Figures 13 and 15, the Strouhal number is based on the cavity length, L, as defined originally by Rossiter, whereas in Figures 14 and 16, the Strouhal number is based on cavity depth, D. For the cases $4M2$ (shear-layer mode) and $4M3$, the second Rossiter mode is dominant, whereas for the cases $4M5$ and $4M6(L4)$ the wake mode is dominant and almost

DOI: 10.1002/fld

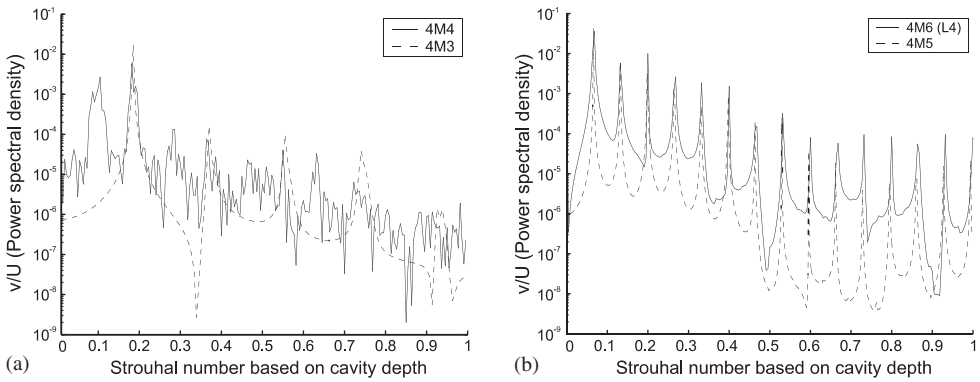

Figure 14. (a) Power spectra of v/U_∞ at a point located at $y = 0$, $x = L - 0.87D$, for the runs $4M3$ and $4M4$; and (b) power spectra of v/U_∞ at the same position for the runs $4M5$ and $4M6(L4)$.

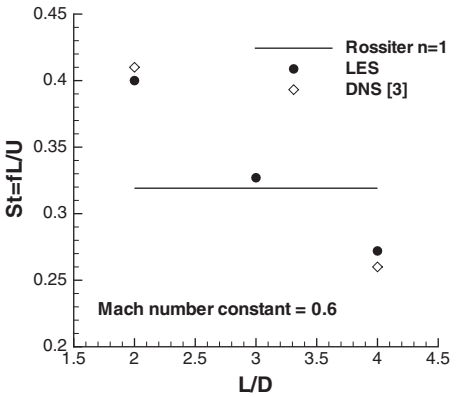

Figure 15. Strouhal numbers for peaks in spectra for the L series of runs, compared to Equation (1) and to DNS results [3].

independent of Mach. No Rossiter modes are visualized in these latter cases, as can be seen in Figure 14(b), where only the frequency of the vortex shedding and its higher harmonics are visible. Krishnamurty [22], detected only one mode of oscillation in his experiments with upstream laminar boundary layers, in the Mach range from 0.4 to 0.8.

Figure 15 is the same as Figure 13 but this time for the 'L' series. In this case, the x-axis represents the parameter L/D. The first Rossiter mode (the only shown) is an horizontal line, since the Mach number is constant, and the parameters γ and k in Equation (1) are also kept constant and equal to those used in Figure 13.

For the cases $L2$ and $L3$ the dominant frequency, identified from the computation, is around the first Rossiter mode. This is the case also in the computations of Rowley [3]. In the run $L4(4M6)$ wake mode is identified, being the frequency of the vortex shedding, the only one present in the spectra. Figure 16 shows the normal velocity spectra for cases $L2$ and $L3$. In the case $L2$, the first Rossiter mode is over estimated, but the spectrum shows a clear dominant frequency, with

DOI: 10.1002/fld

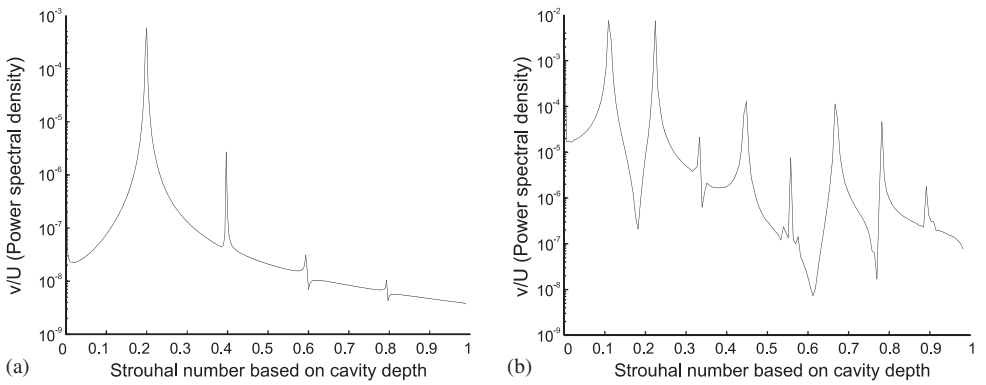

Figure 16. (a) Power spectra of v/U_∞ at a point located at $y = 0$, $x = L - 0.87D$, for the run $L2$; and (b) power spectra of v/U_∞ at the same position for the run $L3$.

several harmonics of decreasing amplitude with the number of the harmonic. This means that just one mode of oscillation (shear) is present in that cavity. In the other hand, in the case $L3$ the first (dominant) peak in the spectrum is very close to the one predicted by the Rossiter formula, but the spectrum is not as clean as in the case $L2$, with a first harmonic with the same amplitude as the dominant frequency and then several other harmonics that do not show a clear tendency in amplitude. This, together with the observation of the time signal in Figure 11, are the reasons why this cavity is marked as oscillating in mixed mode in Table I.

4. CONCLUSIONS

This paper studies the different oscillation modes that may occur in subsonic flows passing over 2D rectangular cavities using a second-order, large eddy simulation code. Like in the DNS simulations from other authors, the computations have revealed three oscillation regimes, shear-layer mode, wake mode and mixed mode. The feedback mechanism for self-sustained oscillations is different in every mode. In shear-layer mode, acoustic scattering from the trailing edge, and receptivity of the shear layer to acoustic disturbances at the leading edge, is responsible for oscillations at the Rossiter frequencies. In wake mode, the feedback mechanism is no longer acoustic, since the frequency of the oscillations is independent of Mach number. The frequencies of oscillation show good agreement with those of other researchers using solvers with higher-order of accuracy (sixth) and resolving much larger domains. For every considered case, the dominant mode of oscillation is clearly predicted. Transition values between the two modes, for the parameter L/θ_0 and for the Mach number have been defined. In the cases where the combination of parameters is such that the flow is in the transition region, second-order schemes seem not enough for accurate predictions. From the quantitative point of view, it seems that the computations are quite sensible to the subgrid scale mode. This is due to the fact that very fine meshes need to be used, to be able to capture acoustic phenomena using low-order schemes. Also, in the opinion of the authors, a dynamic model for the estimation of C_s would help to solve this problem. However, since in cavity flow there are no homogeneous directions, the implementation of such a dynamic model is not straightforward.

DOI: 10.1002/fld

ACKNOWLEDGEMENTS

The authors would like to thank Dr Álvaro Matesanz from the aerodynamics section of Gamesa Eólica for the fruitful discussions during the development of the CFD code. The research work of Wim De Roeck is financed by a scholarship of the Institute for the Promotion of Innovation by Science and Technology in Flanders (IWT).

REFERENCES

1. Rossiter JE. Wind tunnel experiments on the flow over rectangular cavities at subsonic and transonic speeds. Royal Aircraft Establishment, *Technical Report 64037*, 1964.
2. Gharib M, Roshko A. The effect of flow oscillations on cavity drag. *Journal of Fluid Mechanics* 1987; **177**:501–530.
3. Rowley CW. Modeling, simulation, and control of cavity flow oscillations. *Ph.D. Thesis*, California Institute of Technology, 2002.
4. Grace SM. An overview of computational aeroacoustic techniques applied to cavity noise prediction. *AIAA Paper 2001-0510*, 2001.
5. Heller HH, Bliss DB. Aerodynamically induced pressure oscillations in cavities-physical mechanisms and suppression concepts. *Technical Report AFFDL-TR-74-133*, 1975.
6. Komerath NM, Ahuja KK, Chambers FW. Prediction and measurement of flows over cavities—a survey. *AIAA-Paper 82-022*, 1987.
7. Rockwell D, Naudascher E. Self-review—sustained oscillations of flow past cavities. *Journal of Fluids Engineering* 1978; **100**.
8. Gloerfelt X. Bruit Rayonne par un Ecoulement Affleurant une Cavite: simulation Aeroacoustique Directe et Application de Methodes Integrales. *Ph.D. Thesis*, Laboratoire de Mécanique des Fluides et d'Acoustique, École Centrale de Lyon, 2001.
9. Larsson J, Davidson L, Olsson M, Eriksson LE. Aeroacoustic investigation of an open cavity at low Mach number. *AIAA Journal* 2004; **42**(12):2462–2473.
10. De Roeck W, Rubio G, Reymen Y, Meyers J, Baelmans M, Desmet W. Towards accurate flow and acoustic prediction techniques for cavity flow noise applications. *AIAA-Paper 2005-2978*, 2005.
11. Lessani B. Large-eddy simulation of turbulent flows. *Ph.D. Thesis*, Vrije Universiteit Brussel, 2003.
12. Moin P, Squires K, Cabot W, Lee S. A dynamic subgrid-scale model for compressible turbulence and scalar transport. *Physics of Fluids A* 1991; **3**(11):2746–2757.
13. Van Driest ER. On turbulent flow near a wall. *Journal of Aerosol Science* 1956; **23**:1007–1011.
14. Nicoud F, Ducros F. Subgrid-scale modelling based on the square of the velocity gradient tensor. *Flow, Turbulence and Combustion* 1999; **62**:183–200.
15. Germano M, Piomelli U, Moin P, Cabot WH. A dynamic sub-grid scale eddy viscosity model. *Physics of Fluids, A* 1991; **3**:1760–1765.
16. Kim JW, Lee DJ. Generalized characteristic boundary conditions for computational aeroacoustics. *AIAA Journal* 2000; **38**:2040–2049.
17. Poinsot TJ, Lele SK. Boundary conditions for direct simulations of compressible viscous flow. *Journal of Computational Physics* 1992; **101**:104–129.
18. Colonius T, Lele SK, Moin P. Boundary conditions for direct computation of aerodynamic sound. *AIAA Journal* 1993; **31**:1574–1582.
19. Deardorff JW. A numerical study of three-dimensional turbulent channel flow at large Reynols numbers. *Journal of Fluid Mechanics* 1970; **41**(2):453–480.
20. Ziada S, Rockwell S. Oscillations of an unstable mixing layer impinging upon an edge. *Journal of Fluid Mechanics* 1982; **124**:307–334.
21. Sarohia V. Experimental oscillations in flows over shallow cavities. *AIAA Journal* 1977; **15**(7):984–991.
22. Krishnamurty K. Sound radiation from surface cutouts in high speed flow. *Ph.D. Thesis*, California Institute of Technology, 1956.

DOI: 10.1002/fld